

Supplemental material

Air quality measurements in the western Eagle Ford Shale

Geoffrey S. Roest^{1,2,*}, Gunnar W. Schade¹

¹ Department of Atmospheric Sciences, Texas A&M University

² Now at School of Informatics, Computing, and Cyber Systems, Northern Arizona University

* geoffrey.roest@nau.edu

List of Contents

Figure S1. Satellite based flaring detections.

Flaring densities from 2012 to 2016 using data from the VIIRS instrument (Elvidge et al., 2015).

Figure S2. Wind roses for monthly observations at Shape Ranch.

Note that April and November do not have a full month of observations. The increasing frequency of calm observations during the second half of the field campaign was likely affected by aging of the anemometer's bearings.

Figure S3. Wind roses for hourly observations at Shape Ranch.

Wind roses for three-hourly time periods showing the diurnal cycle of winds at Shape Ranch.

Figure S4. The diurnal cycle of CO₂ at Shape Ranch.

Boxplot of CO₂ mixing ratios as a function of hour of day.

Figure S5. Nocturnal CO₂ mixing ratios after precipitation pulses.

Nighttime (00:00 to 06:00 LST) CO₂ mixing ratios were plotted based on the elapsed time since a precipitation pulse of at least 3 mm (0.12 in., Hao et al., 2010). Several extended periods without precipitation occurred.

Figure S6. Comparison of CO, O₃, and NO_x at Shape Ranch and other locations.

A boxplot comparison of CO mixing ratios at Shape Ranch vs. 28 US cities (Baker et al., 2008), maximum daily 8-hour O₃ averages at Shape Ranch vs. the nearby city of Laredo, TX (AQS code 484790016, Texas Commission on Environmental Quality, 2020), and NO_x at Shape Ranch and Karnes City, TX (AQS code 482551070, Texas Commission on Environmental Quality, 2020).

All three pollutants were subset to omit dates outside of the field campaign (10 April to 24 November 2015).

Figure S7. Diurnal variability of NO, NO_x, and NO/NO_x.

The third panel shows evidence of NO₂ photolysis with elevated NO/NO_x ratios during the daytime, while NO emissions quickly react with O₃ at night to form NO₂.

Figure S8. Diurnal variability of selected VOCs.

Boxplot of VOC mixing ratios as a function of hour of day. All units are in ppb.

Figure S9. Comparison of random and SVD seeds on non-negative matrix factorization results.

Three-factor LS-NMF runs with non-negative singular value decomposition (SVD) seed and optimized random seed. Nearly identical factors are produced, though there are noteworthy differences. For example, propene is virtually absent from the second factor of the random seed factorization while it is present in the second factor of the SVD seed. The panels labeled (a) are the first factor (oil and gas field), panels labeled (b) are the second factor (transport/diurnal), and panels labeled (c) represent the third factor (combustion, such as compressor exhaust/flaring).

Figure S10. Alkanes, NO_x, and CO₂ within combustion plumes.

Regressions for the sum of C₃-C₇ alkanes vs. NO_x and CO₂ compared under three conditions: within plumes (defined as NO_x/O₃ > 0.25), during plume “shoulders” (1 hour before and after a plume), and during all other observations. Note that there are fewer data in the alkane vs. NO_x comparison due to the NO_x instrument failure in September 2015. There was a positive correlation between alkanes and both NO_x and CO₂ outside of plumes. However, the ratio is reduced during plume passages, when high NO_x and CO₂ mixing ratios were observed without large co-emissions of alkanes.

Figure S11. VOCs in combustion plumes from 10-13 September 2015.

Regressions for n-butane vs. n-hexane and benzene from 10-13 September 2015 compared under three conditions: within plumes (defined as NO_x/O₃ > 0.25), during plume shoulders, and during all other observations. While uncertainties in the VOC ratios were generally large, a statistically significant difference in n-butane/benzene ratios was observed for in-plume and out-of-plume observations, with relatively higher benzene mixing ratios in plumes.

Figure S12. Similar to Figure S11, but for alkanes, NO_x, and CO₂ within combustion plumes from 10-13 September 2015.

Regressions for the sum of C₃-C₇ alkanes vs. NO_x and CO₂ from 10-13 September 2015 compared under three conditions: within plumes (defined as NO_x/O₃ > 0.25), during plume shoulders, and during all other observations. Like the general plume analysis, there was a positive correlation between alkanes and both NO_x and CO₂ outside of plumes. However, the ratio was greatly reduced during plumes, when higher NO_x and CO₂ mixing ratios were observed, indicating distinct combustion plumes without a significant co-emission of alkanes. However, the uncertainties for the slopes remained large.

Figure S13. NO_x and CO₂ enhancements for a plume on 17 July 2015.

A distinct cluster of observations with elevated NO_x enhancements and relatively stable CO₂ enhancements is indicative of high-temperature combustion emissions.

Figure S14. NO_x and CO₂ enhancements for a plume on 10 September 2015.

Several brief plumes of very high NO_x enhancements and smaller CO₂ enhancements is indicative of emissions from a nearby high-temperature combustion source. The high NO_x/CO₂ ratios during these brief plumes were not identified by the screening method due to the large cluster of data points with lower NO_x/CO₂ enhancements.

Table S1. Technical information for the trace gas measurements.

Table S2. Columns used in the dual-channel GC-FID analysis.

Table S3: Summary of meteorology at Shape Ranch (top) in 2015, compared to 1981-2010 climatology for Carrizo springs.

Text S1. Description of measurements.

References

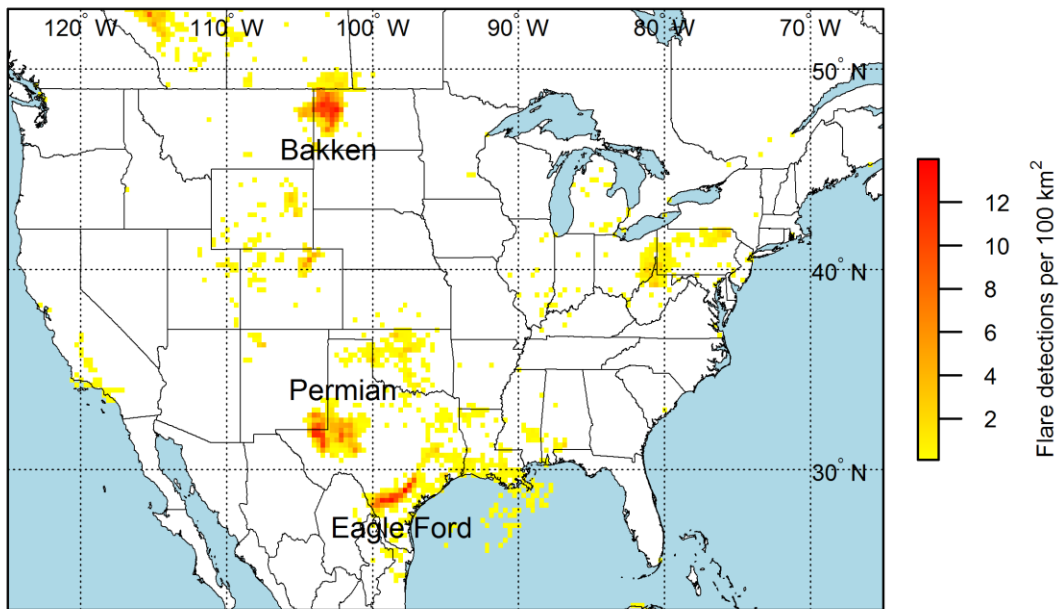


Figure S1. Satellite based flaring detections.

Flaring densities from 2012 to 2016 using data from the VIIRS instrument (Elvidge et al., 2015).

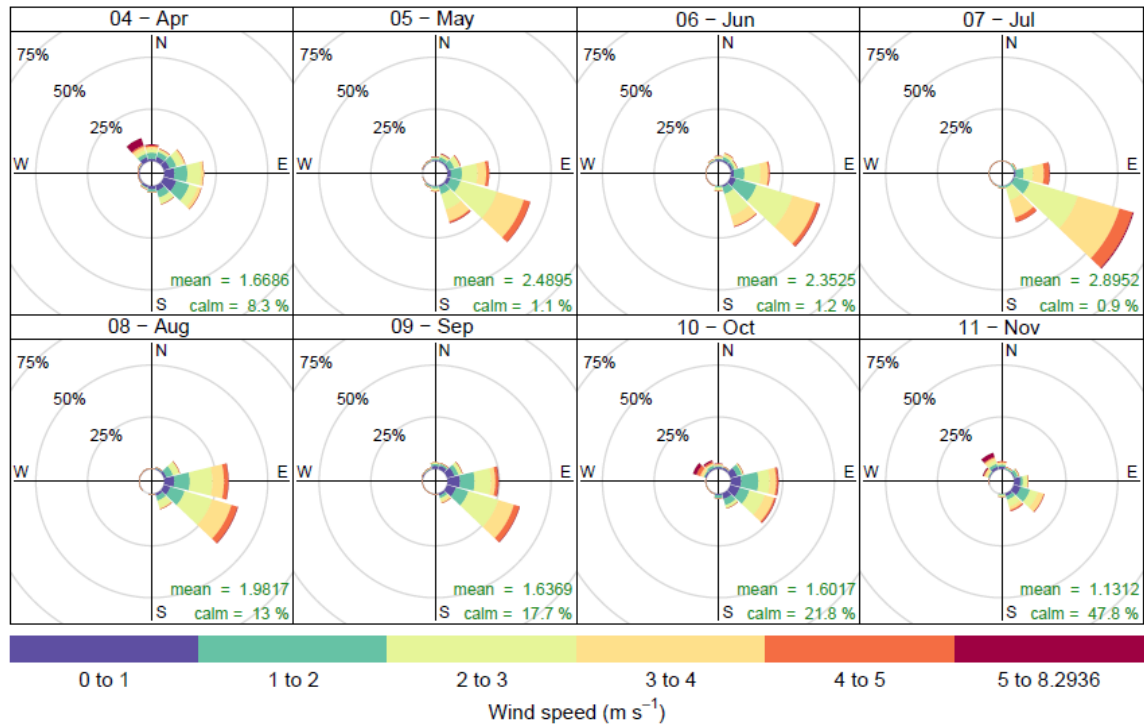


Figure S2. Wind roses for monthly observations at Shape Ranch.

Note that April and November do not have a full month of observations. The increasing frequency of calm observations during the second half of the field campaign was likely affected by aging of the anemometer's bearings.

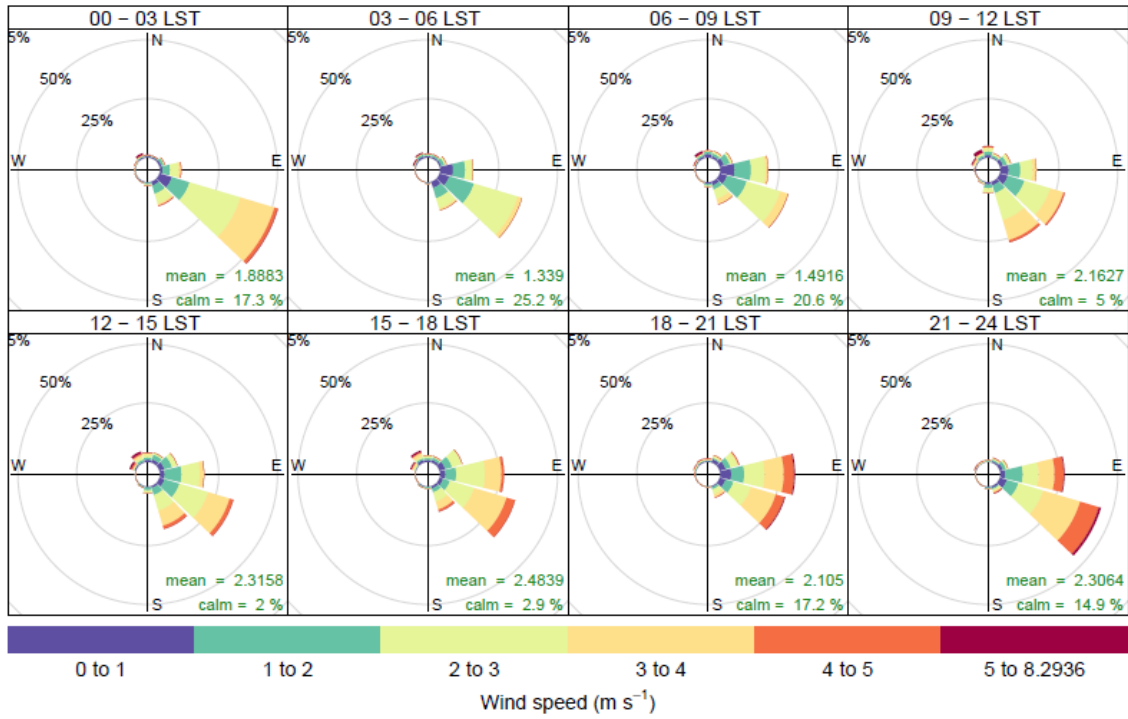


Figure S3. Wind roses for hourly observations at Shape Ranch.

Wind roses for three-hourly time periods showing the diurnal cycle of winds at Shape Ranch.

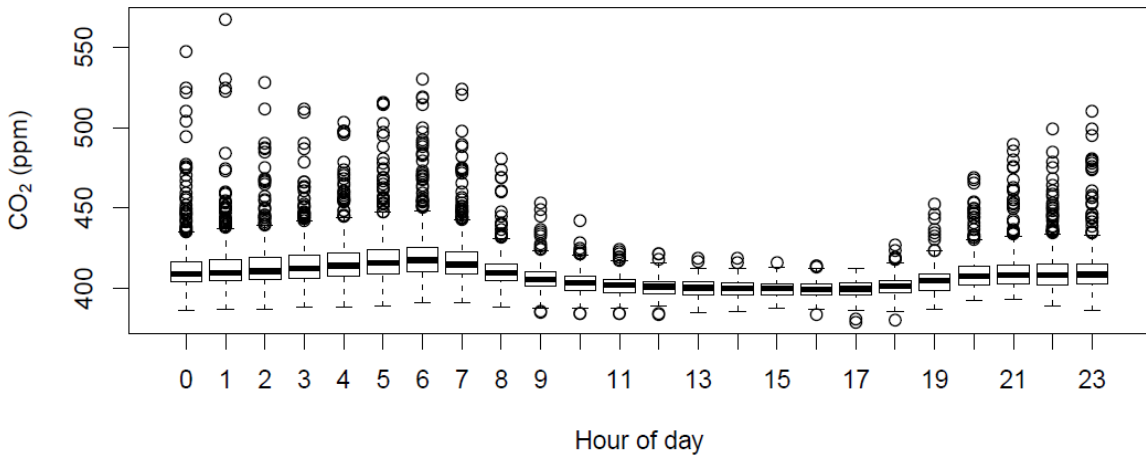


Figure S4. The diurnal cycle of CO₂ at Shape Ranch.

Boxplot of CO₂ mixing ratios as a function of hour of day.

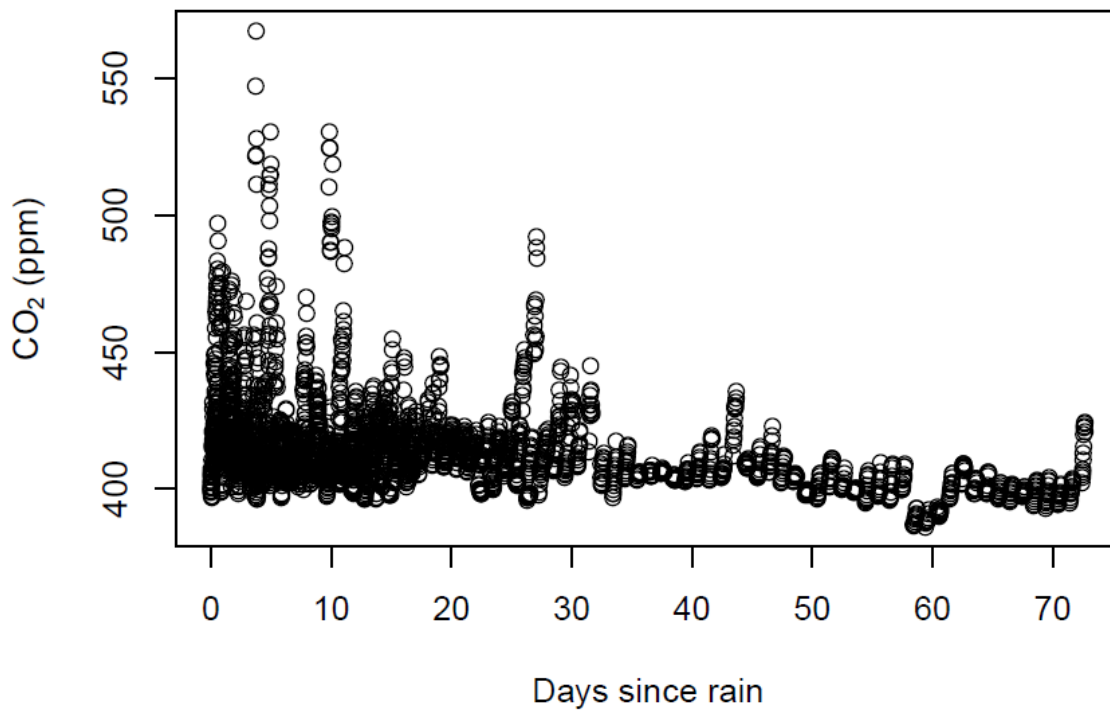


Figure S5. Nocturnal CO₂ mixing ratios after precipitation pulses.

Nighttime (00:00 to 06:00 LST) CO₂ mixing ratios were plotted based on the elapsed time since a precipitation pulse of at least 3 mm (0.12 in., Hao et al., 2010). Several extended periods without precipitation occurred.

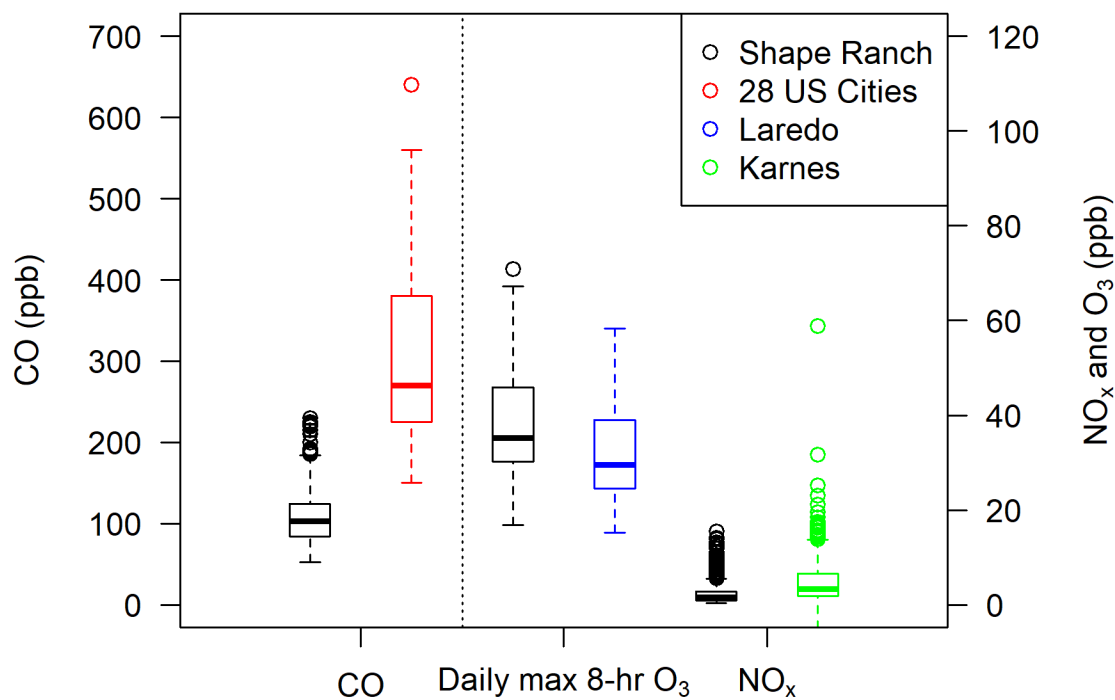


Figure S6. Comparison of CO, O₃, and NO_x at Shape Ranch and other locations.

A boxplot comparison of CO mixing ratios at Shape Ranch vs. 28 US cities (Baker et al., 2008), maximum daily 8-hour O₃ averages at Shape Ranch vs. the nearby city of Laredo, TX (AQS code 484790016, Texas Commission on Environmental Quality, 2020), and NO_x at Shape Ranch and Karnes City, TX (AQS code 482551070, Texas Commission on Environmental Quality, 2020). All three pollutants were subset to omit dates outside of the field campaign (10 April to 24 November 2015).

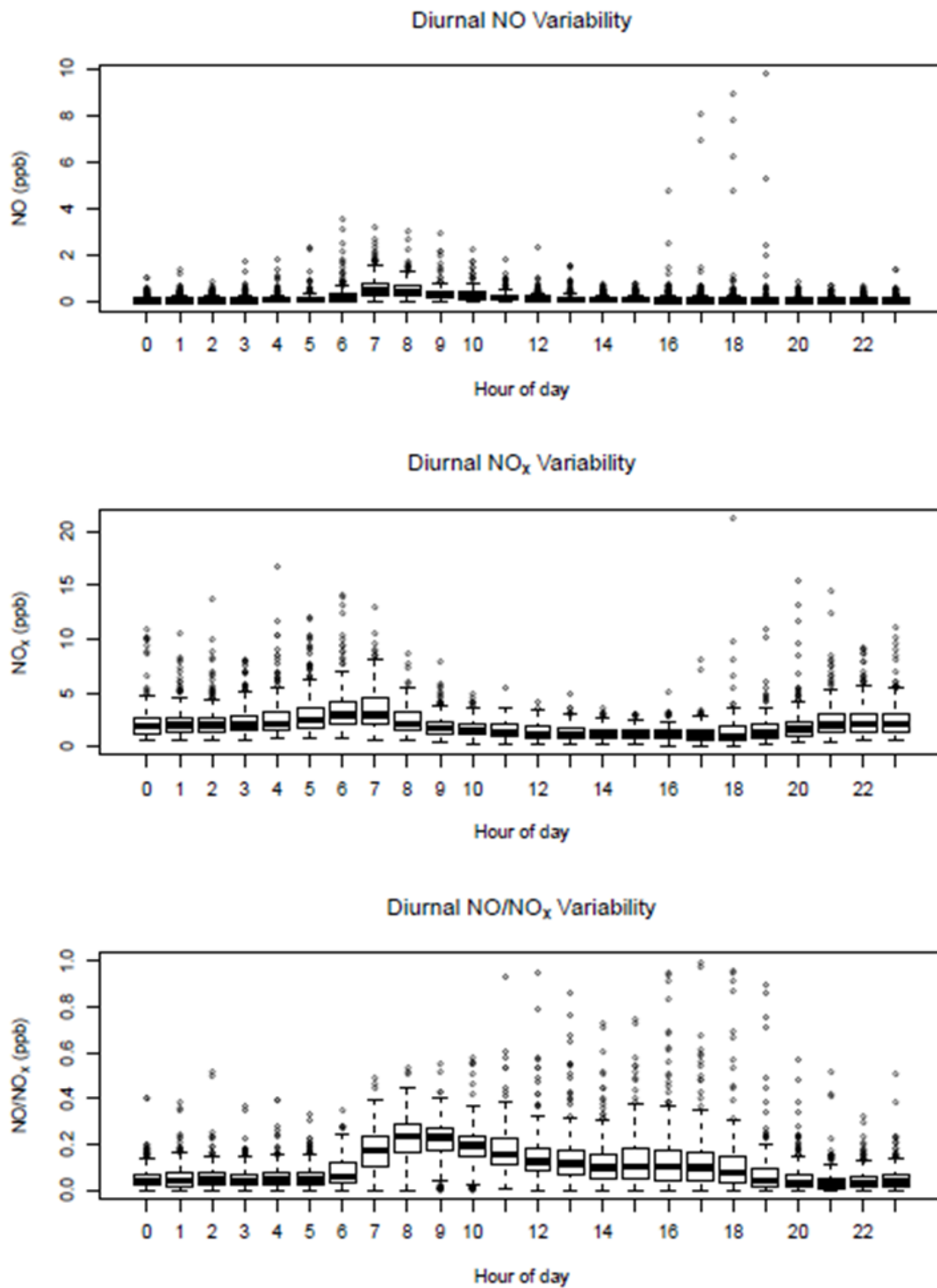


Figure S7. Diurnal variability of NO, NO_x, and NO/NO_x.

The third panel shows evidence of NO₂ photolysis with elevated NO/NO_x ratios during the daytime, while NO emissions quickly react with O₃ at night to form NO₂.

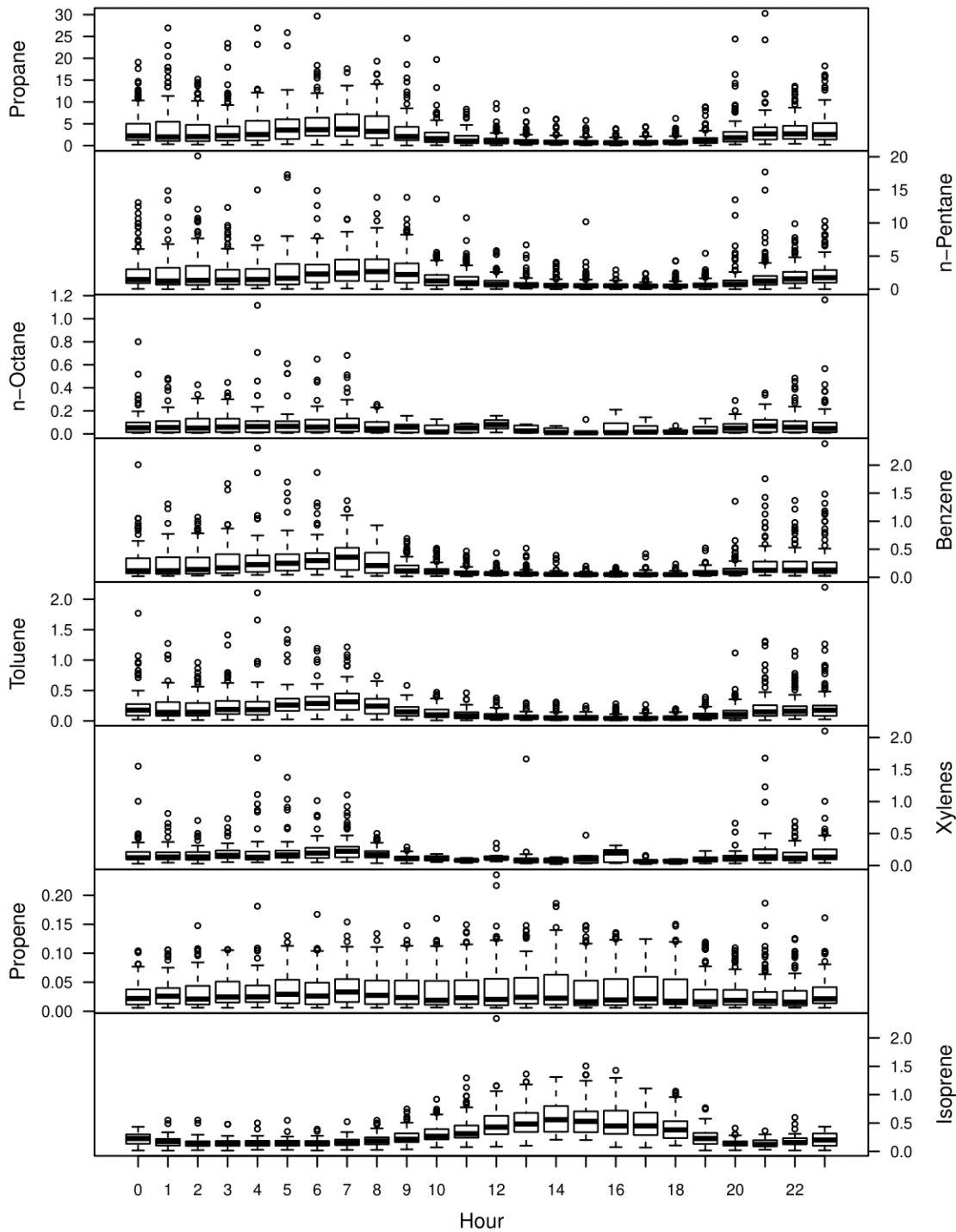


Figure S8. Diurnal variability of selected VOCs.

Boxplot of VOC mixing ratios as a function of hour of day. All units are in ppb.

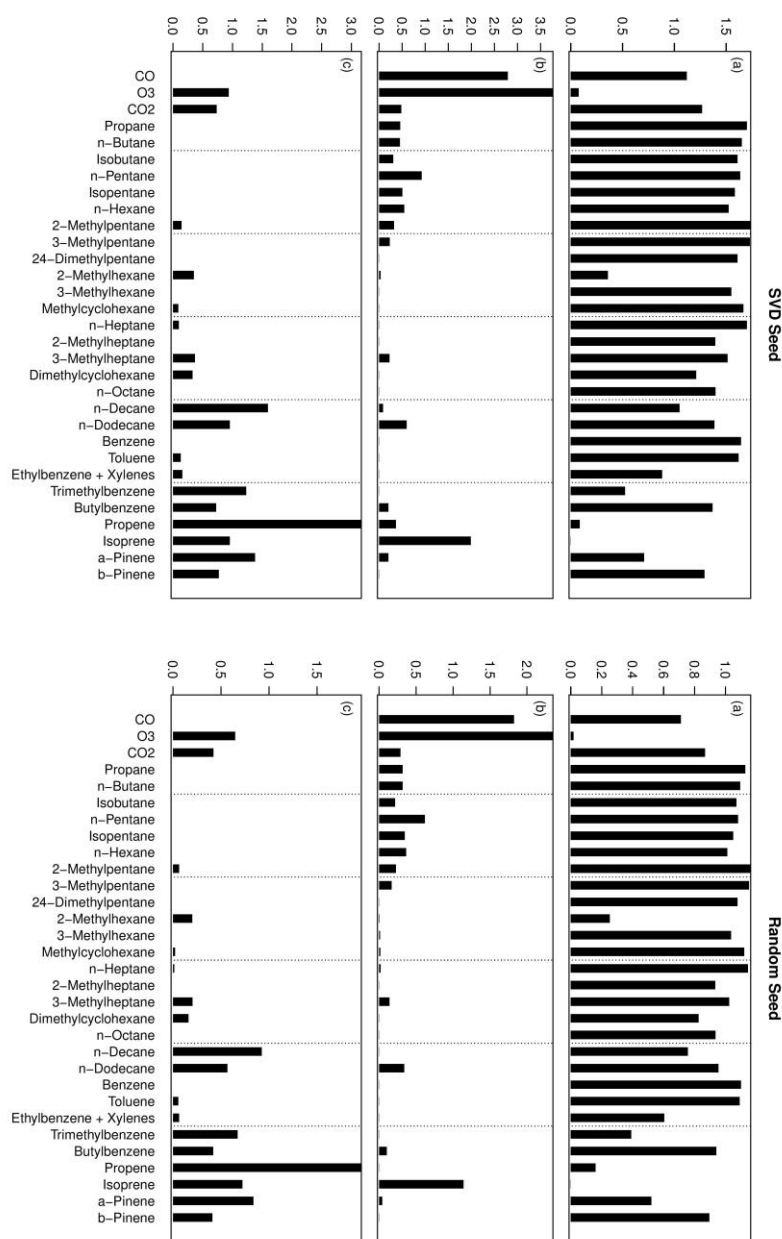


Figure S9. Comparison of random and SVD seeds on non-negative matrix factorization results.

Three-factor LS-NMF runs with non-negative singular value decomposition (SVD) seed and optimized random seed. Nearly identical factors are produced, though there are noteworthy differences. For example, propene is virtually absent from the second factor of the random seed factorization while it is present in the second factor of the SVD seed. The panels labeled (a) are the first factor (oil and gas field), panels labeled (b) are the second factor (transport/diurnal), and panels labeled (c) represent the third factor (combustion, such as compressor exhaust/flaring).

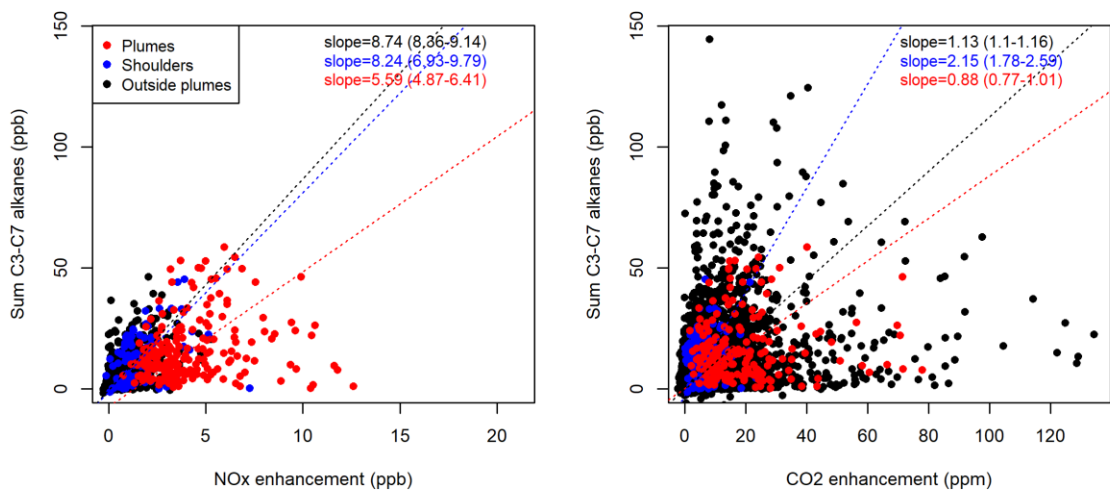


Figure S10. Alkanes, NO_x, and CO₂ within combustion plumes.

Regressions for the sum of C₃-C₇ alkanes vs. NO_x and CO₂ compared under three conditions: within plumes (defined as NO_x/O₃ > 0.25), during plume “shoulders” (1 hour before and after a plume), and during all other observations. Note that there are fewer data in the alkane vs. NO_x comparison due to the NO_x instrument failure in September 2015. There was a positive correlation between alkanes and both NO_x and CO₂ outside of plumes. However, the ratio is reduced during plume passages, when high NO_x and CO₂ mixing ratios were observed without large co-emissions of alkanes.

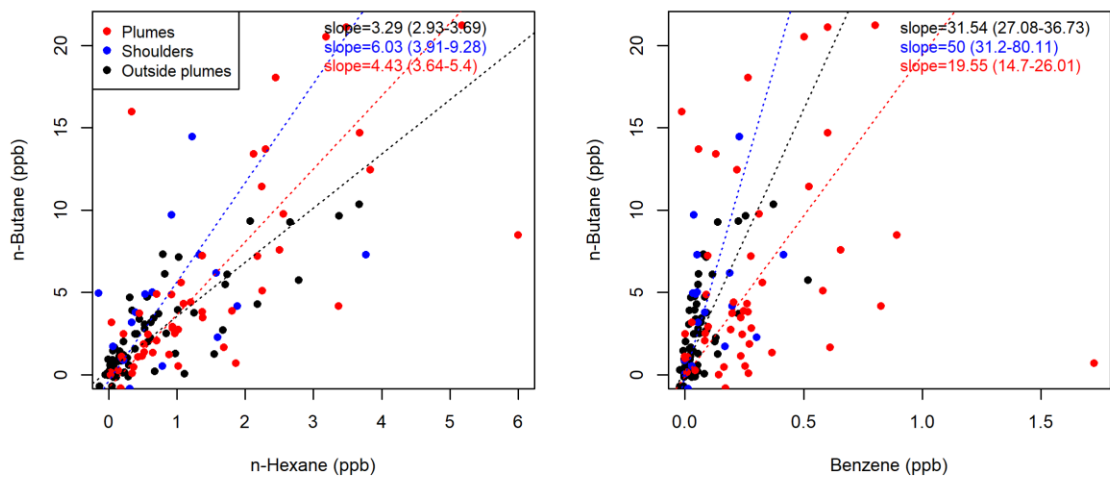


Figure S11. VOCs in combustion plumes from 10-13 September 2015.

Regressions for n-butane vs. n-hexane and benzene from 10-13 September 2015 compared under three conditions: within plumes (defined as $\text{NO}_x/\text{O}_3 > 0.25$), during plume shoulders, and during all other observations. While uncertainties in the VOC ratios were generally large, a statistically significant difference in n-butane/benzene ratios was observed for in-plume and out-of-plume observations, with relatively higher benzene mixing ratios in plumes.

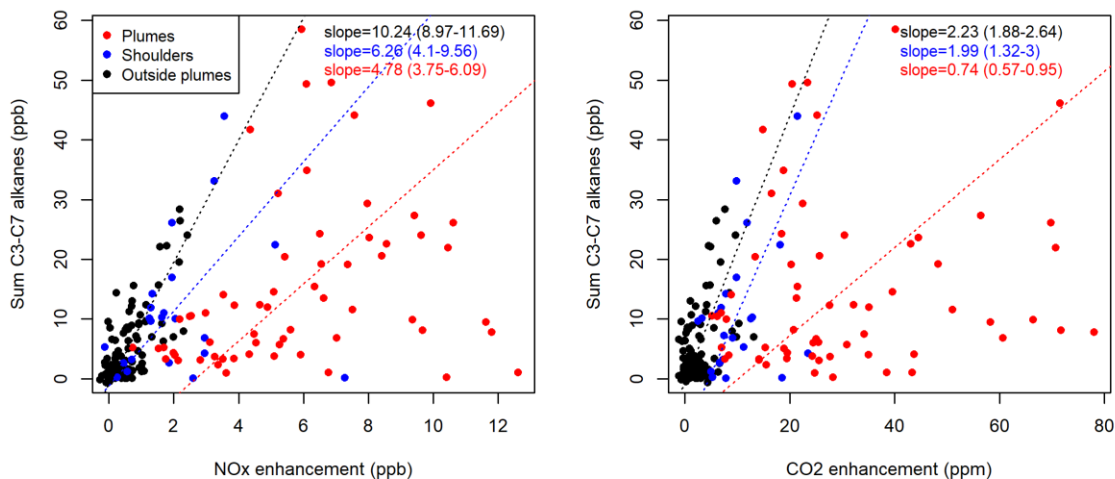


Figure S12. Similar to Figure S11, but for alkanes, NO_x, and CO₂ within combustion plumes from 10-13 September 2015.

Regressions for the sum of C₃-C₇ alkanes vs. NO_x and CO₂ from 10-13 September 2015 compared under three conditions: within plumes (defined as NO_x/O₃ > 0.25), during plume shoulders, and during all other observations. Like the general plume analysis, there was a positive correlation between alkanes and both NO_x and CO₂ outside of plumes. However, the ratio was greatly reduced during plumes, when higher NO_x and CO₂ mixing ratios were observed, indicating distinct combustion plumes without a significant co-emission of alkanes. However, the uncertainties for the slopes remained large.

Event on 2015-07-17

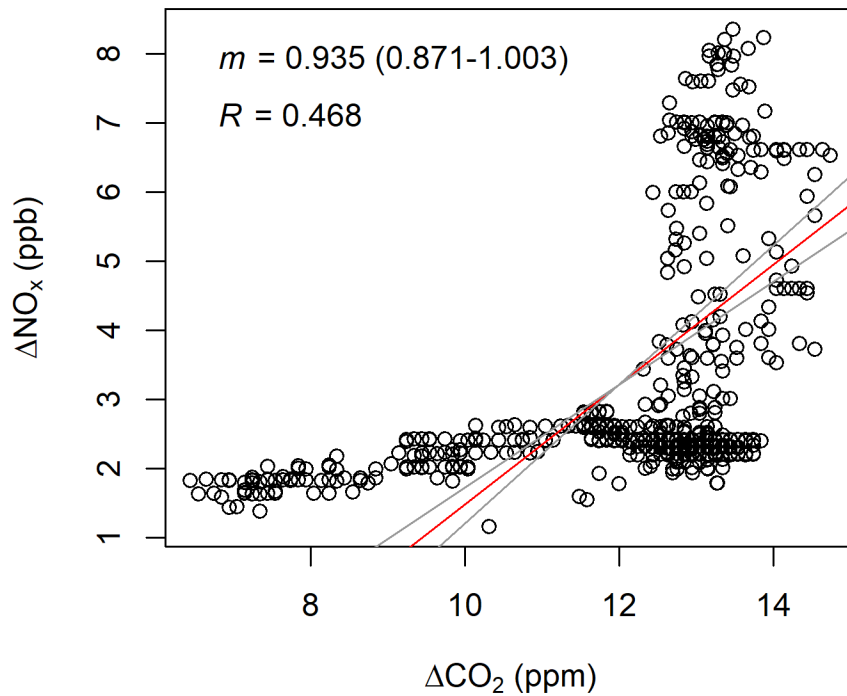
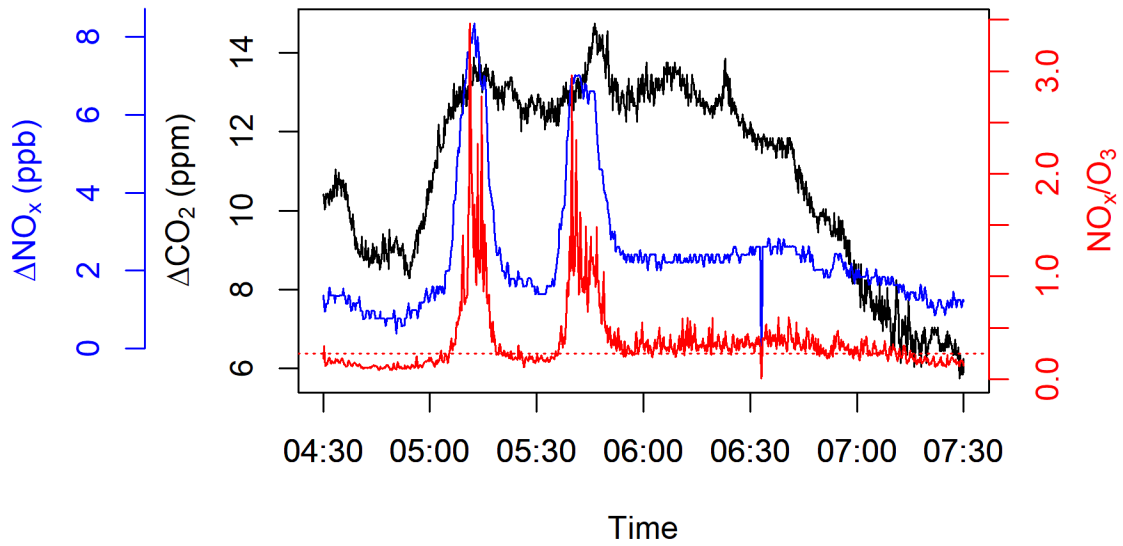


Figure S13. NO_x and CO_2 enhancements for a plume on 17 July 2015.

A distinct cluster of observations with elevated NO_x enhancements and relatively stable CO_2 enhancements is indicative of high-temperature combustion emissions.

Event on 2015-09-10

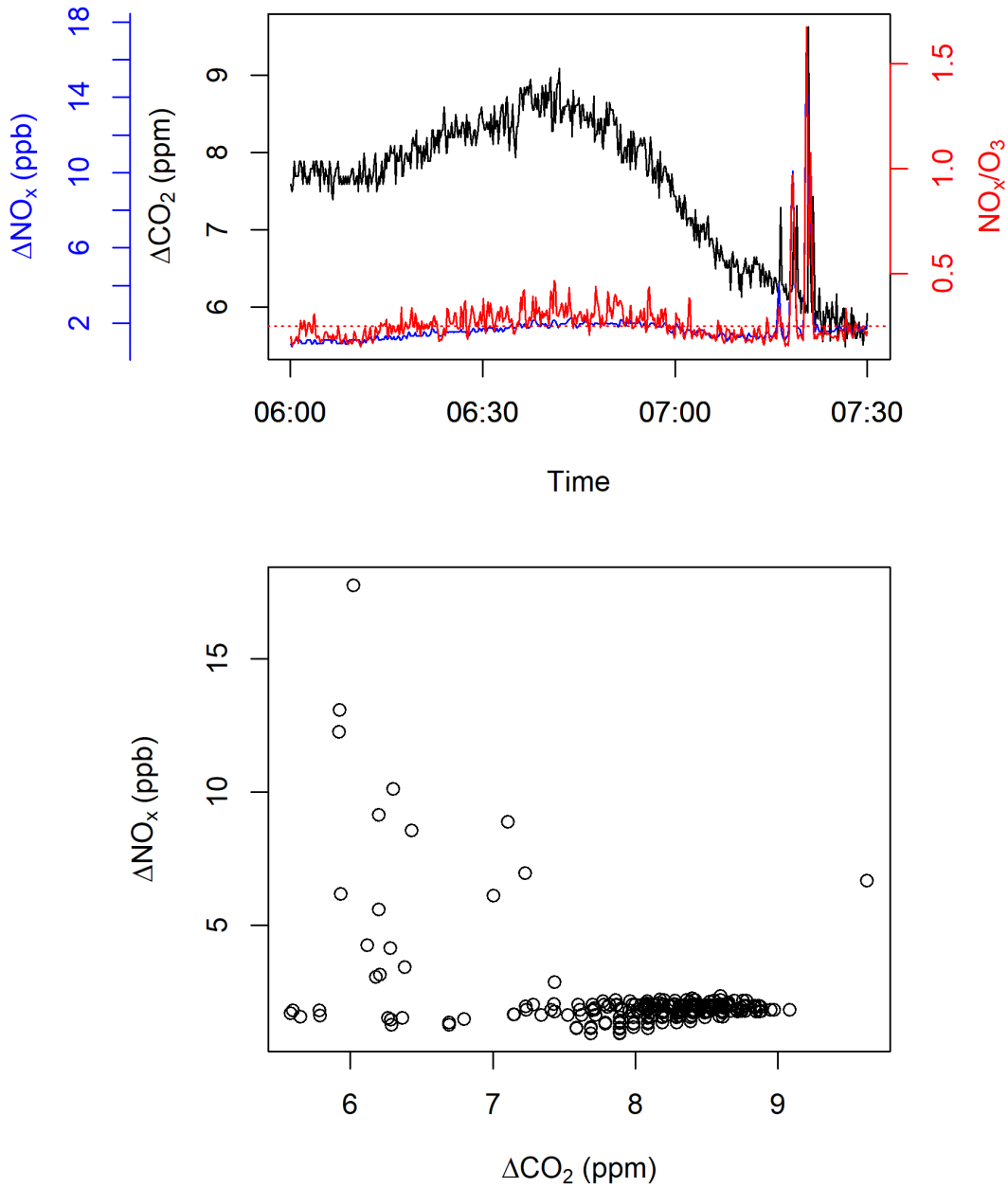


Figure S14. NO_x and CO_2 enhancements for a plume on 10 September 2015.

Several brief plumes of very high NO_x enhancements and smaller CO_2 enhancements is indicative of emissions from a nearby high-temperature combustion source. The high NO_x/CO_2 ratios during these brief plumes were not identified by the screening method due to the large cluster of data points with lower NO_x/CO_2 enhancements.

Table S1. Technical information for the trace gas measurements.

Gas	Instrument	LoD	Precision	Accuracy	Zero/Calibration
NO/NO _x	Thermo Electron Corp. Model 42C	0.4 ppb	± 0.4 ppb	-	zero: CO in zero air standard* span: NO standard* at 103.5 ppb ±5%
CO	Thermo Electron Corp. Model 48C	40 ppb	± 20 ppb	-	zero: internal catalytic zero every 6 h span: CO in zero air standard* at 547 ppb ±2%
CO ₂	Licor Model 840A	0 ppm	RMS noise < 1 ppm	± 1% of reading	zero: CO in zero air standard* CO ₂ in zero air standard* at 454 ppm ±1%
H ₂ O		0 ‰	RMS noise < 0.01 ‰	± 1.5% of reading	zero: CO in zero air standard* span: Factory calibration
O ₃	2BTech Model 202	3 ppb	± 1.5 ppb or ± 2% of reading, whichever is greater		external zero using ozone scrubber Factory calibration
Hydrocarbons	SRI model 8610c GC w/ dual-channel FID	~0.07 ppbC	± 1.8% for internal standard	± 7.3% **	Zero air generator 2,2-Dimethylbutane in N ₂ standard at 20.52 ppm ±2%

* Standard gases form Scott Marrin Inc.

** 5% accuracy for each of two flow meters and 2% accuracy for standard gas mixing ratio, added in quadrature.

Table S2. Columns used in the dual-channel GC-FID analysis.

Column	Target Compounds	Polarity	Length	Inner Diameter
MTX-624	BTEX, C ₆₊ hydrocarbons	Low to mid	60 m	0.53 mm
PLOT-A1	Short chain alkanes up to C ₆	Non-polar	30 m	

Table S3: Summary of meteorology at Shape Ranch (top) in 2015, compared to 1981-2010 climatology for Carrizo springs (bottom, Arguez et al., 2010).

	Month	April*	May	June	July	August	September	October	November*
Observed	Average daily max temp (°C)	28.4	31.2	34.5	38.3	39.8	37.5	33.2	26.4
	Average daily mean temp (°C)	22.7	25.7	28.2	31.2	32.2	30.0	26.1	20.3
	Average daily min temp (°C)	17.7	21.1	22.8	24.1	24.4	23.1	19.8	14.8
	Monthly precip (mm)	20.1	67.8	68.3	0.3	0.0	13.7	57.2	38.4
Climatology	Average daily max temp (°C)	29.6	32.8	35.7	36.6	37.2	33.7	29.3	23.8
	Average daily mean temp (°C)	22.4	26.2	29.3	30.1	30.4	27.2	22.5	16.7
	Average daily min temp (°C)	15.3	19.6	22.9	23.7	23.8	20.8	15.7	9.7
	Monthly precip (mm)	40.4	71.6	52.3	49.8	38.9	61.5	53.8	28.4

* April and November temperatures and precipitation at Shape Ranch are based on an incomplete month of measurements.

Text S1. Description of measurements.

The meteorology and trace gas dataset being used for this analysis is the half-hourly data discussed in section 2. Data for O₃, CO₂, and H₂O are available for the entire time period from 9 April to 24 November 2015, except for bad data points and calibrations. The CO analyzer failed on 8 November due to a fading infrared light source, while the NO_x analyzer failed on 15 September due to an electrical issue. Hydrocarbon mixing ratios have sparse data availability before 29 July when an electrical issue in the trailer was corrected. Electronic spikes occurred as UPCs turned on or off during significant drops in the voltage of the trailer's power source. While this issue was rectified in July, voltage drops were a recurring problem during the first portion of the field campaign, especially when the air conditioner went through a power cycle on hot afternoons. After 6 October, when one of the hydrocarbon trap heaters failed, the two hydrocarbon channels were alternated to collect periods of data for all hydrocarbons in the dataset.

Data were removed as power issues in the trailer resulted in the failure of the hydrogen generator, which extinguished the flames in the FIDs, or sampling periods or thermal desorption were interrupted. Other data were flagged for removal, including a number of runs after the instrument was started to allow for the traps to be cleaned, and zero runs and injections of standard gases performed.

Hydrocarbons were identified in the laboratory and in the field via retention times using injections of standard gases from Scotty transportable cylinders, and/or knowledge of expected hydrocarbons in a rural, continental oil and gas field environment. Gases that were not included in standard injections were tentatively identified based on their relative retention times. This introduces some uncertainty as compounds cannot be identified with FIDs, and some compounds may coelute, such as, e.g. n-octane and toluene. Furthermore, temperature fluctuations in the trailer impacted the retention times of more volatile compounds as the column oven was not always able to cool to the set start temperature (40 °C). Breakthrough of short-chain hydrocarbons, such as propane and propene, were assessed by examining the propane peaks for tailing and by testing the ratios of injected alkanes and alkenes at near-ambient to above-ambient mixing ratios. No issues with breakthrough were identified. Shifting retention times were addressed by integrating chromatographic peaks in small batches and adjusting expected retention times as needed.

An internal standard gas containing 2,2-dimethylbutane (“neohexane”, prepared in March 2015 by Scott Marrin Inc., CA; 20.52 ppm ± 2% in N₂) was used to quantify hydrocarbon mixing ratios. This compound was chosen as its atmospheric mixing ratio was expected to be very small, its retention time known, and its elution nearly unaffected by other hydrocarbons. The period from 17-25 September 2015 was selected to calculate chromatographic performance using the internal standard peak because there was continuous, uninterrupted data collection. During this period, the internal standard was introduced at 2 mL min⁻¹ at the head of the main sampling line, where the net flow was approximately 1430 mL min⁻¹, resulting in the internal standard being diluted to 28.1 ppb (168.6 ppbC). The variability of the chromatographic peaks for the internal standard provided an estimated precision of ± 1.8% (2σ). The uncertainty in the internal standard mixing ratio of ± 2% and the precision of the two flow meters (± 5% each) assessing standard and main line flows, resulted in an estimated hydrocarbon measurement uncertainty of ± 8% (± 13.5 ppbC for the internal standard) when added in quadrature.

For FIDs, it is assumed that the instrument response is a function of the number of carbons and the relative mass of carbon within the molecule (Lamanna and Goldstein, 1999). Thus, the relative response factor of a compound is:

$$\text{RRF}_i = \frac{n_{C,i} \cdot F_i}{n_{C,IS} \cdot F_{IS}} \quad (1)$$

where $n_{C,i}$ and $n_{C,IS}$ are the number of carbon atoms in an arbitrary species i and the internal standard, respectively, and F_i and F_{IS} are the fractions of carbon by mass. The mixing ratio of each species was then calculated as

$$X_i = \frac{A_i \chi_{IS}}{\text{RRF}_i A_{IS}} \quad (2)$$

where A_i is the area of each chromatogram peak for species i , A_{IS} is the mean area of the internal standard peaks from 17-25 September 2015, and $\chi_{IS} = 28.1$ ppb is the corresponding mixing ratio of the internal standard. The limit of detection corresponded to a chromatographic peak with an area of 1 (as determined by PeakSimple), which is equivalent to approximately 0.07 ppbC.

References

- Arguez, A., Durre, I., Applequist, S., Squires, M., Vose, R., Yin, X., Bilotta, R., 2010. U.S. Climate Normals Product Suite (1981-2010). <https://doi.org/10.7289/V5PN93JP>
- Baker, A.K., Beyersdorf, A.J., Doezema, L.A., Katzenstein, A., Meinardi, S., Simpson, I.J., Blake, D.R., Sherwood Rowland, F., 2008. Measurements of nonmethane hydrocarbons in 28 United States cities. *Atmospheric Environment* 42, 170–182. <https://doi.org/10.1016/j.atmosenv.2007.09.007>
- Elvidge, C., Zhizhin, M., Baugh, K., Hsu, F.-C., Ghosh, T., 2015. Methods for Global Survey of Natural Gas Flaring from Visible Infrared Imaging Radiometer Suite Data. *Energies* 9, 14. <https://doi.org/10.3390/en9010014>
- Hao, Y., Wang, Y., Mei, X., Cui, X., 2010. The response of ecosystem CO₂ exchange to small precipitation pulses over a temperate steppe. *Plant Ecology* 209, 335–347. <https://doi.org/10.1007/s11258-010-9766-1>
- Lamanna, M.S., Goldstein, A.H., 1999. In situ measurements of C₂ - C₁₀ volatile organic compounds above a Sierra Nevada ponderosa pine plantation. *Journal of Geophysical Research: Atmospheres* 104, 21247–21262. <https://doi.org/10.1029/1999JD900289>
- Texas Commission on Environmental Quality, 2020. Data by Year by Site by Parameter [WWW Document]. URL https://www.tceq.texas.gov/cgi-bin/compliance/monops/yearly_summary.pl?cams=1070 (accessed 1.30.20).